Fully 3D list-mode time-of-flight PET image reconstruction on GPUs using CUDA

Jing-yu Cui
Department of Electrical Engineering, Stanford University, Stanford, California 94305

Guillem Pratx
Department of Radiation Oncology, Stanford University, Stanford, California 94305

Sven Prevrhal
Philips Healthcare, San Jose, California 95134

Craig S. Levin[a)]
Departments of Radiology, Electrical Engineering, Physics, and Molecular Imaging Program at Stanford (MIPS), Stanford University, Stanford, California 94305

(Received 31 May 2011; revised 28 September 2011; accepted for publication 22 October 2011; published 1 December 2011)

Purpose: List-mode processing is an efficient way of dealing with the sparse nature of positron emission tomography (PET) data sets and is the processing method of choice for time-of-flight (ToF) PET image reconstruction. However, the massive amount of computation involved in forward projection and backprojection limits the application of list-mode reconstruction in practice, and makes it challenging to incorporate accurate system modeling.

Methods: The authors present a novel formulation for computing line projection operations on graphics processing units (GPUs) using the compute unified device architecture (CUDA) framework, and apply the formulation to list-mode ordered-subsets expectation maximization (OSEM) image reconstruction. Our method overcomes well-known GPU challenges such as divergence of compute threads, limited bandwidth of global memory, and limited size of shared memory, while exploiting GPU capabilities such as fast access to shared memory and efficient linear interpolation of texture memory. Execution time comparison and image quality analysis of the GPU-CUDA method and the central processing unit (CPU) method are performed on several data sets acquired on a preclinical scanner and a clinical ToF scanner.

Results: When applied to line projection operations for non-ToF list-mode PET, this new GPU-CUDA method is >200 times faster than a single-threaded reference CPU implementation. For ToF reconstruction, we exploit a ToF-specific optimization to improve the efficiency of our parallel processing method, resulting in GPU reconstruction >300 times faster than the CPU counterpart. For a typical whole-body scan with $75 \times 75 \times 26$ image matrix, 40.7 million LORs, 33 subsets, and 3 iterations, the overall processing time is 7.7 s for GPU and 42 min for a single-threaded CPU. Image quality and accuracy are preserved for multiple imaging configurations and reconstruction parameters, with normalized root mean squared (RMS) deviation less than 1% between CPU and GPU-generated images for all cases.

Conclusions: A list-mode ToF OSEM library was developed on the GPU-CUDA platform. Our studies show that the GPU reformulation is considerably faster than a single-threaded reference CPU method especially for ToF processing, while producing virtually identical images. This new method can be easily adapted to enable more advanced algorithms for high resolution PET reconstruction based on additional information such as depth of interaction (DoI), photon energy, and point spread functions (PSFs). © *2011 American Association of Physicists in Medicine*.
[DOI: 10.1118/1.3661998]

Key words: PET image reconstruction, time-of-flight PET, list-mode, OSEM, CUDA, GPU, line projections, high performance computing, acceleration

I. INTRODUCTION

Positron emission tomography (PET) image reconstruction methods based on list-mode acquisition have many advantages compared with those using sinograms, especially for time-of-flight (ToF),[1–3] high resolution,[4,5] and dynamic[6] PET data. List-mode data can be reconstructed using iterative algorithms such as maximum likelihood expectation maximization (MLEM) (Ref. 7) and ordered-subsets expectation maximization (OSEM).[8–12] However, these algorithms require forward and backprojection between individual lines of response (LORs) and voxels and, therefore, have much higher computational cost. For example, it requires tens of minutes up to hours of CPU time to reconstruct a typical 3D PET image, even on high-end CPUs with highly optimized algorithms.[3,13,14] Yet, within a cycle of forward and back-projection, LORs can be processed independently, allowing data-parallel processing on multiprocessor hardware.

Programmable graphics processing units (GPUs) have emerged as a popular alternative to multi-CPU computer clusters for high performance computation because of potential savings of cost, space, and power.[15] A significant research effort has been devoted to exploiting GPU technology for x-ray computed tomography (CT),[16,17] digital tomosynthesis,[18] radiation treatment planning,[19] dose calculation,[20] and other medical physics applications.[21] Compared with multi-CPU clusters,[22] the faster speed and lower cost of communication between GPU cores makes scaling easier for applications that involve internode communication. This is true for most of the iterative algorithms, which require the result of the previous step to be broadcasted to all the nodes before the next iteration can begin.

In a previous article, we reported a GPU formulation of 3D list-mode OSEM using the OpenGL graphics library.[13] Using a graphics library for general-purpose parallel computing has several drawbacks: The code is difficult to develop and maintain since the algorithm must be implemented as a graphics rendering process; performance may be compromised by the lack of access to all the capabilities of the GPU, for example, shared memory; and code portability is a challenge because the graphics code needs to be customized for specific graphics cards for best performance.

In this paper, we present our recent work in reformulating and accelerating fully 3D list-mode ToF PET image reconstruction on GPUs using the compute unified device architecture (CUDA) framework.[23]

CUDA makes the highly parallel architecture of the GPU cores available to the developers in a C-like programming paradigm.[23] Compared to OpenGL, CUDA gives the programmer direct access to GPU features that are not available from OpenGL, such as shared memory, thus, potentially could be more efficient for certain applications. Briefly, the execution model organizes individual threads into thread blocks. The significance of a thread block is that its members can communicate through fast block-specific shared memory, whereas threads in different blocks run independently. If interblock communication is necessary, it must use much slower off-chip global memory. Atomic operations and thread synchronization primitives are further provided to allow threads in each thread block to coordinate memory access and execution. CUDA code has sufficient flexibility to manipulate the scheduling of the computation, yet the programmer does not need to be concerned with the details of the hardware implementation since they are automatically handled by the run-time environment. Once the CUDA code is written, it can run on future graphics cards, automatically exploiting their advanced capability without requiring code modifications.

We reformulated the OSEM algorithm to map it efficiently to the NVIDIA Fermi GPU architecture and the CUDA framework. When applied to line projection operations for non-ToF list-mode PET, this method is >200 times faster than a single-threaded reference CPU implementation. For ToF reconstruction, since each LOR intersects fewer voxels, the method is greater than 300-fold faster than the CPU counterpart. Image quality and quantification are preserved with negligible difference between CPU and GPU-generated images.

This paper describes detailed formulations to enable 3D list-mode OSEM acceleration using the GPU-CUDA platform. This formulation can be applied to any PET and single photon emission computed tomography (SPECT) system configuration. In this work, we mainly focus on exploiting this novel technique for image reconstruction for ToF-PET. The contributions of this formulation are as follows:

(1) Spatial and temporal locality is exploited by caching the image volume in faster shared memory and reformulating the projections to access the image slice-by-slice.
(2) LORs are partitioned into groups according to their orientations, thus, the intersection of the tube of response (TOR) and the slice has a fixed footprint, which can be accessed using a fixed-bound for-loop to avoid GPU thread divergence.
(3) For ToF reconstruction, events are further sorted according to their ToF centers to reduce unnecessary computation.
(4) The list-mode data are organized into structure of arrays (SoA) in the global memory to enable coalesced parallel access from different GPU threads.
(5) For forward projection, a line-driven approach with no data race condition is proposed, with the sparseness of the system matrix exploited.
(6) For backprojection, the pros and cons of the line- and voxel-driven approaches are analyzed and discussed, and the selected line-driven approach with hardware atomic operations is presented because it exploits the sparseness of the system matrix, while having relatively small overhead imposed by the atomic operations.
(7) Multiplicative update is performed on the GPU *in situ* without additional CPU-GPU communication.
(8) Several other optimizations are utilized, including free interpolation of the texture memory, loop unrolling, fast math, etc.
(9) The proposed method is a general framework which can be easily adapted to incorporate more information such as depth of interaction (DoI), photon energy, and point spread functions (PSFs) into the image reconstruction algorithm.

II. MATERIALS AND METHODS

II.A. Image reconstruction

The MLEM algorithm[7] can be used to reconstruct a tomographic image based on a set of projective measurements. The iterative algorithm can be summarized as

$$\mathbf{x}^{(k+1)} = \mathbf{x}^{(k)} \circ \frac{\mathbf{1}}{A^T\mathbf{1}} \circ \left(A^T \frac{\mathbf{y}}{A\mathbf{x}^{(k)} + \mathbf{c}} \right), \quad (1)$$

where A is the system matrix, whose elements A_{ij} denote the probability that a positron decay occurring in the jth voxel gets detected in the ith LOR; $\mathbf{y}$ is the LOR measurement; $\mathbf{c}$ is the additive correction term, usually the sum of the estimated scatter correction $\mathbf{s}$ and random correction $\mathbf{r}$; $\mathbf{x}^{(k)}$ is the image estimate at the k th step; $\circ$ is the Hadamard (element-wise) product, and $\div$ is the element-wise division. In the OSEM algorithm,[8] only a subset of all LORs are used for each update. For list-mode OSEM,[10] the subsets are usually time-ordered, and $\mathbf{y} = \mathbf{1}$.

The system matrix A is usually very big.[24,25] Researchers have been working on reducing its size by exploiting its sparse and symmetric structures.[26–28] Several alternatives exist for calculating the system matrix on-the-fly, including Siddon's[29] and Joseph's method.[30] However, theses methods are limited to thin, ideal lines that do not accurately represent the physics of the photon detection in PET. Instead, we use a TOR approach to represent PET projective measurement because it provides more flexibility for accurately modeling the system response. In this paper, the shape of the system response is modeled using a shift-invariant kernel. It is a straightforward extension of this work to change the innermost loop of the algorithm to incorporate a shift-varying kernel.

II.B. Reformulation and implementation for the CUDA platform

The bottleneck of iterative reconstruction algorithms lies in the forward and backprojection operations that are responsible for calculating the summed contributions of all voxels to all LORs, and the summed contributions of all LORs to all voxels, respectively. Both operations are intrinsically parallel, but in order to implement the algorithm efficiently on the GPU, special consideration is required to match the computation to the hardware architecture.

Some key principles for efficient CUDA programming include increasing arithmetic intensity, that is the ratio of arithmetic to memory operations; hiding global memory latency by maximizing thread occupancy, which let the scheduler replace threads waiting for memory transactions with ready threads; using caches, texture memory, and shared memory; ensuring thread coherence to avoid serialization of diverging execution paths; and minimizing the use of atomic operations, which are required to guarantee correctness in the presence of data race conditions.

In Secs. II B 1-II B 11, we will introduce the steps we took to formulate and implement the MLEM and OSEM algorithms to run efficiently on GPUs.

II.B.11. Global memory layout

We layout the data structure in GPU global memory in such a way that the memory accesses of threads within a half-warp are coalesced into one transaction, thereby preserving global memory bandwidth. More specifically, a *structure of arrays* (SoA) instead of an *array of structures* (AoS) is used to store data elements of events.[23] The first data element of all events is stored in a continuous block of memory, followed by the second element of all events, and so forth.

II.B.2. Caching with shared memory

Projection operations typically have low arithmetic intensity: they access a large number of voxels and LORs but only perform simple calculations with them. This fact suggests that global memory access is a bottleneck of the algorithm, and must be reduced as much as possible.

Because all LORs access the same image volume, we cache the image in the fast shared memory, and reuse it for all LORs in the same thread block. Since the memory footprint of the reconstructed volume currently far exceeds the total amount of shared memory (e.g., 16 kB per streaming multiprocessor for GTX 280, and up to 48 kB for GTX 480), we process the image volume slice-by-slice. As shown in Fig. 1, within each thread block, threads work in parallel to load a slice of the image into shared memory. All threads in a thread block perform the computations related to the slice in fast shared memory, calculating the intersections between the TORs and the voxels in the current slice.

If a slice does not fit into shared memory, it is further divided into tiles, which are processed sequentially.

II.B.3. Line partitioning

In the proposed method, given that an event is observed in a LOR, the distribution of the possible annihilation location is described by the coincident detector response function (CDRF),[31] which has a "tube" shape proportional to the detector size. A Gaussian or Bessel function is used to approximate the CDRF. A cylindrical TOR is chosen to include all the voxels whose contribution to the CDRF is above a certain threshold. The intersection of the TOR and a slice is an ellipse (Fig. 2). To account for all the voxels in the ellipse, a double for-loop was used to traverse all the voxels contained within the rectangle bounding the ellipse. However, for different relative orientations of the TOR and the slice, the width of the bounding rectangle can vary from the diameter T_w of the TOR (when the TOR and the slice are orthogonal) to the size of the slice (when the TOR and the slice are parallel) (Fig. 2); hence, slice-by-slice processing of

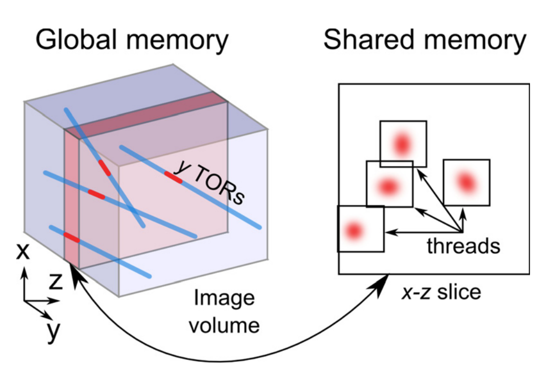

FIG. 1. Illustration of the caching mechanism of the proposed GPU-CUDA method.

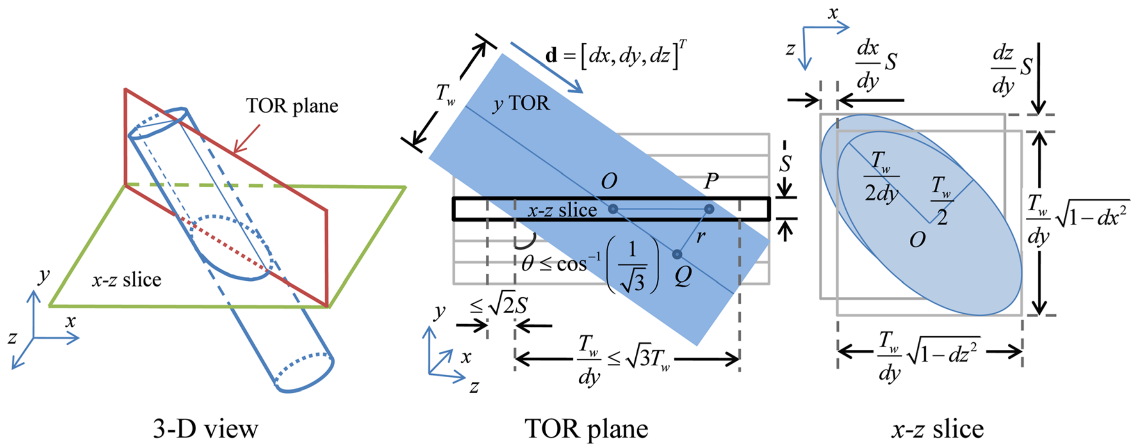

FIG. 2. By slicing the image volume orthogonal to the predominant TOR direction, the area of the intersection between the TOR and the slice is bounded. Here, a *y* direction TOR and *x*-*z* slice are shown as an example.

the TORs will introduce severe thread divergence, serializing the calculations on the GPU.

In order to prevent the execution of the threads from diverging within thread blocks, we categorize the lines within each subset into three classes according to their predominant direction. More specifically, the predominant direction is the direction selected from *x, y*, and *z* that has the largest absolute value of inner product with the line direction. Here directions *x* and *y* span the transaxial image plane, and direction *z* is along the scanner axis. For each class of lines, the slices are selected to be orthogonal to the predominant line direction. For example, for lines whose predominant direction is along *y*, the slice is chosen to be parallel to the *x*-*z* plane (Fig. 1). This categorization step can be performed very efficiently on the GPU using the partition primitive,[23] which partitions a set of items into two groups based on the output of a binary function, for example, whether or not the predominant direction of an LOR is *x*. This step needs to be performed only once for all the iterations with very small time cost. For example, on a GTX 480 GPU, it takes 12 ms to categorize 1 million randomly-generated LORs.

By slicing the image volume orthogonally to the predominant TOR direction, the area of the intersection of the TOR and the slice is bounded. For example, in Fig. 2, the TOR has unit direction $\mathbf{d} = [dx,\ dy,\ dz]^T$ satisfying $|dy| \geq |dx|$ and $|dy| \geq |dz|$, so the predominant direction is *y*, and *x*-*z* slices are used. In the TOR plane, the angle θ between the TOR and the *y* axis is equal to arccos (dy), which is always smaller than $\arccos\left(\frac{1}{\sqrt{3}}\right) = 54.7°$, so the long axis of the ellipse resulting from the TOR-slice intersection is no larger than $\sqrt{3}T_w$, where T_w is the width of the TOR. Considering the thickness of the slice being S, the intersection of the TOR with the upper and lower boundaries of the slice are two ellipses offset in the long axis direction by tan (θ) S, which is smaller than $\sqrt{2}S$. In the *x*-*z* plane, the size of the bounding box of the intersection is $\left(\frac{dx}{dy}S + \frac{T_w}{dy}\sqrt{1-dz^2}\right) \times \left(\frac{dz}{dy}S + \frac{T_w}{dy}\sqrt{1-dx^2}\right)$, which is smaller than $W \times W$, where $W = \sqrt{2}T_w + S$. Therefore, we can simply process a fixed square region of $W \times W$ voxels for all TORs without introducing any thread divergence.

II.B.4. Projection kernel calculation

For the TOR model considered in the work, the calculation of the projection kernel involves two steps: calculation of the distance *r* between the center of a voxel to the LOR, and calculation of the weighting function *f*(*r*).

For example, using the geometry of Fig. 2, the distance *r* from a certain point *P* in the current *x*-*z* slice to the LOR satisfies

$$r^2 = \|PQ\|_2^2 = \|PO\|_2^2 - \langle PO, \mathbf{d}\rangle^2, \tag{2}$$

where $\mathbf{d} = (dx,\ dy,\ dz)$ is the unit direction of the LOR, and $PO = (\Delta x,\ 0,\ \Delta z)$ with the second element being zero since we are using the *x*-*z* slice.

Equation (2) can be further simplified as

$$r^2 = \Delta x^2 + \Delta z^2 - (\Delta x dx + \Delta z dz)^2, \tag{3}$$

which takes three additions and five multiplications to calculate.

The calculation of *f*(*r*) is performed by mapping the function to a 1D texture with *M* elements in CUDA. Note that linear interpolation is freely available to improve the accuracy of the representation. In our experiments, we find that $M = 2048$ is sufficient.

For simple weighting functions such as Gaussian kernels, the speed of the texture lookup is comparable to the speed of direct computation. When images are represented using blob basis functions,[32] the weighting function is more complicated and the texture mapping method demonstrates great advantage in terms of speed. This strategy can be applied to other parameterizations of the TOR as long as the weighting function only depends on the distance *r*. The TOR can be also parameterized with other variables. For a detailed discussion of alternative projection strategies and their implications, please refer to Ref. 33.

II.B.5. Forward projection

Forward projections of LORs are independent of each other. As a result, LORs are divided into equal-sized groups, each assigned to a thread block. Each thread in the thread block processes a line independently as shown in Algorithm 1. Because the computation tasks are divided according to the output, this step is a gather operation[34] and there is no data race condition.

If the image is represented using multiple sets of basis functions, for example using two sets of blobs arranged in even–odd body-centered cubic (BCC) grids,[32] the forward projection accumulates values from both grids into the same set of LORs.

Algorithm 1: Line-driven forward projection kernel for each thread

---

for each slice **do**
  All threads load the current slice into the shared memory in parallel
  Synchronize threads in current block
  for each line assigned to the current thread **do**
    Calculate and accumulate the contribution of current slice to the line
    Write line value to global memory (can be deferred after looping over all slices if there is enough register or shared memory space for storing the line values)
  end for
  Synchronize threads in current block
end for

II.B.6. Backprojection

To avoid data races, backprojection must be performed as a gather operation, i.e., the computation must be distributed according to the voxels. However, because the interactions of the TORs and the voxels are very sparse, and the list-mode events are not ordered, this method would launch many empty threads, and the computational efficiency would suffer.

In our method, we use a line-driven scheme similar to the forward projection. In this case, multiple lines may write to the same location in shared memory simultaneously, so atomic operations must be used to ensure correctness of the reconstructed image. The floating point atomic operations are available in hardware in the Fermi architecture, and can be implemented in software for GPUs that do not support hardware floating point atomic operations. The backprojection algorithm is detailed in Algorithm 2.

While atomic operations introduce overhead on memory transactions, in our experience, this approach is substantially more efficient than the voxel-driven approach. Figure 3 shows the number of collisions for backprojecting 1 million randomly-generated lines. Collisions happen relatively rarely (0.2% of all memory writes for random TORs), and the measured overhead is less than 10% compared to using regular write operations.

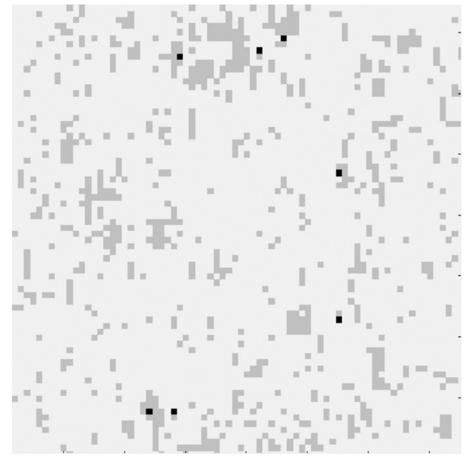

FIG. 3. Number of collisions per voxel for backprojecting a random set of 1 million lines. White means no collision, gray means one collision, and black means two collisions.

If the image is represented using multiple sets of basis functions, for example using two sets of blobs arranged in even–odd BCC grids, backprojection is performed for all grids.

Algorithm 2: Line-driven backprojection kernel for each thread

---

for each slice **do**
  All threads load the current slice into the shared memory in parallel
  Synchronize threads in current block
  for each line assigned to the current thread **do**
    Calculate and atomically accumulate the contribution of the line to the slice in the shared memory
  end for
  Synchronize threads in current block
  All threads write the current slice back to the global memory in parallel
  Synchronize threads in current block
end for

II.B.7. Time-of-flight projections

If ToF information is available, the weighting function is the product of the non-ToF weighting function and a Gaussian function that is centered at the event ToF center and extends along the TOR direction. The variance of the Gaussian function is set to be proportional to the time resolution of the system.

ToF information increases the sparseness of the system matrix. As a result, the number of voxels contributing to each TOR is further reduced. As shown in Fig. 4, although all four LORs intersect with the current slice, only LORs 2 and 3 contribute to it significantly.

To exploit this property, we sort the events within each predominant direction group according to the position of the corresponding ToF center along the predominant direction. For example, the events in the x group are sorted according to the x component of their ToF centers. As a result, the threads within a thread block, which are executed in a single-instruction-multiple-data (SIMD) fashion, can all skip loading a slice if it does not intersect with any of the ToF lines they are processing. This strategy greatly reduces unnecessary calculations for voxels and ToF TORs that are too far from each other, and results in a 36% reduction of the execution time (Fig. 5). Note that this event sorting process is very efficiently performed on the GPU, and needs to be performed only once for all iterations of the ToF reconstruction. For example, to sort 1, 2, 3, 4, and 5 million randomly-generated LORs on a GTX 480 GPU, it takes 64, 110, 162,

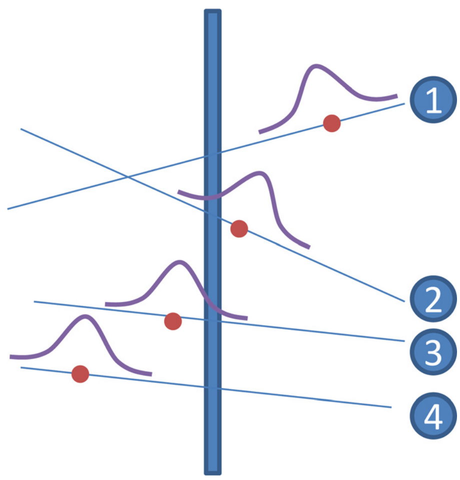

FIG. 4. With the ToF information, fewer LOR-slice pairs need to be processed. Four LORs are shown intersecting the current slice. The dots on each line denote the ToF center, and the bell shapes denote the ToF kernels. Only LORs 2 and 3 contribute to the current slice significantly.

210, and 262 ms, respectively. The complexity of the sorting algorithm is $O(nlogn)$, where n is the number of LORs being sorted.

II.B.8. Multiplicative update

In the multiplicative update step, the previously estimated image is multiplied by two matrices element-wise: the back-projection result $A^T\frac{\mathbf{y}}{A\mathbf{x}^{(k)}+\mathbf{c}}$, and the precomputed element-wise reciprocal of the normalization map $\frac{1}{A^T\mathbf{1}}$. These two matrices were preloaded on the GPU, so this step requires no data transfer between the CPU and GPU, and take a negligible portion of the total execution time.

Note that multiplying the image by $\frac{1}{A^T\mathbf{1}}$ and dividing it by $A^T\mathbf{1}$ are mathematically equivalent. However, when the normalization map $A^T\mathbf{1}$ contains zeros or very small values, dividing by $A^T\mathbf{1}$ will be numerically unstable. This can be easily fixed if we use the first method, and set the corresponding values in $\frac{1}{A^T\mathbf{1}}$ to zero.

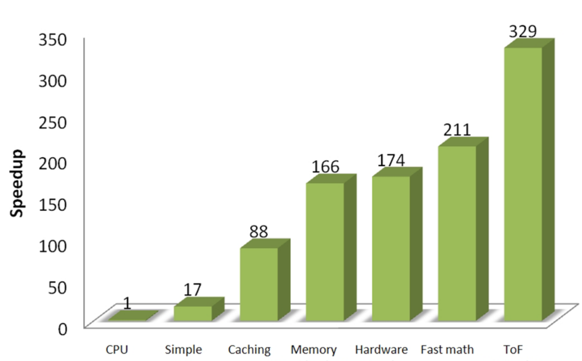

FIG. 5. Cumulative contributions of different optimization strategies to the overall speedup of the GPU-CUDA method compared to the CPU-based code. Simple GPU implementation refers to the method that directly maps the computation to the GPU hardware without using the subsequent optimizations listed in this figure.

II.B.9. Fast math

NVIDIA GPUs have intrinsic arithmetic operations implemented in hardware. These operations perform common arithmetic computations faster but less accurately. This feature can be activated through the compiler flag `nvcc − use_fast_math`. Our experiment shows that enabling fast math marginally affects the final image accuracy, while saving computation time depending on the size of the TOR.

II.B.10. Loop unrolling

Loop unrolling can reduce the number of dynamic instructions by avoiding extra comparisons and branches. It provides additional opportunities for instruction level parallelism since more independent instructions are exposed. However, aggressive unrolling can introduce more static instructions and higher register usage; the former increases the instruction load time, and the latter forces some of the registers to be spilled to L1 cache or global memory. The *#pragma unroll* compiler directive informs the compiler of potential loops to be unrolled, and the compiler decides whether or not to unroll based on the trade-offs above.

II.B.11. Bank conflicts

CUDA shared memory is organized in equal-sized memory banks. Any n simultaneous memory accesses that fall into n different banks can be served simultaneously, while memory accesses in the same bank have to be serialized.

No bank conflicts occur when image slices are transferred from global memory to shared memory, since for 32-bit floating point numbers, no two threads access the same memory bank simultaneously as long as the stride s is an odd number:[23]

```
__shared__float shared[];
shared[offset + s * threadIdx.x] = some_value;
```

However, when projection operations access the cached image slice in shared memory, the access pattern is not regular, and bank conflicts are inevitable to some extent. But even with bank conflicts, the main bottleneck for the GPU-CUDA method remains the global memory access, and the penalty imposed by slight bank conflict is negligible.

II.C. Evaluation

II.C.1. CPU and GPU hardware

We compare the speed of the GPU-CUDA method with a baseline CPU implementation running in single thread mode on an Core 2 Duo E6600 2.4 GHz CPU (Intel, Santa Clara, CA, 2006). Of note, the baseline CPU implementation is not part of or equivalent to the manufacture's product.

The GPU-CUDA code runs on a GeForce GTX 480 GPU (NVIDIA, Santa Clara, CA, 2010), with 480 programmable cores grouped into 15 streaming multiprocessors (SMs), running at 1.45 GHz clock frequency. The GPU has 1.5 GB on-board memory, accessible from the CPU via the PCI-E 2.0 $\times$ 16 bus. For comparison, the GPU-CUDA implementation was also run on a GeForce GTX 285 GPU (NVIDIA, Santa Clara, CA, 2009), with 240 programmable cores grouped into 30 SMs, running at 1.45 GHz clock frequency. Compared with the GTX 480, the GTX 285 has only 1 GB of on-board memory, and hardware floating point atomic operations are not available. The CUDA driver and runtime 3.2 are used to access the functionalities of both GPUs.

II.C.2. Processing time analysis

The processing time for the CPU and GPU-CUDA methods are measured. For the GPU-CUDA method, contributions of different optimization strategies are analyzed. Important parameters of the GPU-CUDA method, such as the size of the thread block and the number of thread blocks, are varied to analyze their impact on the performance.

II.C.3. Imaging experiments and reconstruction parameters

A cylindrical hot rod phantom (Micro Deluxe phantom, Data Spectrum, Durham, NC), comprising rods of different diameters spaced by twice their diameter (1.2, 1.6, 2.4, 3.2, 4.0, and 4.8 mm) was filled with 110 μCi of radioactive solution of $Na^{18}F$, and 25.3 million events were acquired on a GE eXplore Vista DR system[35] for 20 min. A $103 \times 103 \times 36$ volumetric image of $0.65 \times 0.65 \times 0.65$ mm^3 voxels was reconstructed using the list-mode 3D OSEM algorithm with 2 iterations and 40 subsets, both on the GPU and on the CPU. For simplicity, the data corrections for photon scatter, random coincidences, photon attenuation, and detector efficiency normalization were not applied.

A mouse was injected with $Na^{18}F$, a bone tracer, and 28.8 million events were acquired on the GE eXplore Vista DR system.[35] Reconstruction of a $72 \times 72 \times 51$ image with 1 mm^3 voxels was performed with three iterations and five subsets of list-mode OSEM using the CPU and the GPU. For simplicity, no data corrections were applied.

A clinical whole-body scan acquired on a Philips Gemini TF 64 PET/CT scanner[36] was also reconstructed after acquiring 40.7 million events with ToF information. Consistently with the vendor's standard reconstruction method, the image was represented using two sets of $75 \times 75 \times 26$ blob basis functions[32] of radius 2.5 mm, and reconstructed using 33 subsets and 3 iterations. The time resolution is 636 ps. The Gaussian ToF kernel is truncated at 3 times the standard deviation. Corrections for photon scatter, random events, photon attenuation, and normalization were applied.

For all experiments, the voxel-by-voxel difference between the images generated using the GPU and the CPU is measured using the normalized root mean squared (RMS) deviation, which is defined as the RMS divided by the range of the voxel values. The contrast between two regions of interest (ROIs) is calculated as the ratio of the mean voxel value in the two ROIs. The noise of a ROI is calculated as the standard deviation of the voxel values in it.

III. RESULTS

III.A. Processing time

The GPU execution time for backprojection, forward projection, and multiplicative update of 1 million random LORs in a $75 \times 75 \times 26$ image using the CUDA-GPU method is 95 ms for non-ToF reconstruction, and 61 ms for ToF reconstruction. This is >200 times faster than the reference CPU-based code for non-ToF, and >300 times faster for ToF. A breakdown of the contributions of the different optimization steps is shown in Fig. 5. Note that reducing the cost of memory transactions plays the most important role among all the contributions.

To analyze the performance of the GPU-CUDA method on different hardware, we report the number of non-ToF and ToF events that can be processed per second for different GPU configurations as a function of the thread block size in Fig. 6.

In order to measure the scalability of the GPU-CUDA method, we generate data sets with varying numbers of lines, and list timing results in Table I. We fit the data to a linear model $T = aN + b$, where N is the number of events in millions, T is execution time in milliseconds. The fitted parameters for GTX 480 with block size 1024 and grid size 15 are $a = 59.77$ ms/million LOR and $b = 2.31$ ms, with goodness of fit $r^2 = 0.9999$.

We also investigate the impact of using fast math on speed and image quality. We report the execution time and the normalized RMS deviation between two images reconstructed with and without fast math for different TOR sizes in Table II. Using fast math results in faster execution with virtually no change in image quality.

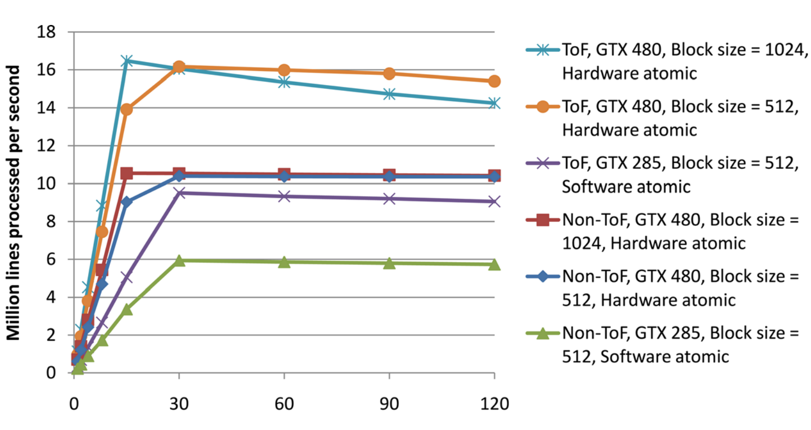

FIG. 6. Number of randomly-generated LORs that can be processed per second, as a function of the number of thread blocks for the GPU-CUDA method. Due to hardware limitations, block size of GTX 285 cannot be set to 1024.

TABLE I. Execution time (ms) for processing varying numbers of randomly-generated LORs for the GPU-CUDA method.

	GPU	Block size	Grid size	# LORs processed (million) 1	2	5	10
ToF	GTX 480	1024	15	61	122	301	600
			30	63	123	302	601
		512	15	74	145	360	719
			30	62	121	298	594
	GTX 285	512	15	218	403	1004	2005
			30	108	213	527	1053
Non-ToF	GTX 480	1024	15	95	190	475	949
			30	98	192	476	950
		512	15	109	220	549	1109
			30	97	192	481	962
	GTX 285	512	15	296	590	1471	2939
			30	168	333	828	1654

To understand how the algorithm scales with more voxels in the image and bigger TOR, detailed analysis is performed and the results are presented in Tables III–V. When the number of the voxels in the reconstructed image increases, we keep the physical dimension of the TOR constant by increasing the number of voxels in the TOR, and the execution time as a function of image size is shown in Table III. We also show the execution time for varying number of voxels in the reconstructed image while fixing the other parameters in Table IV, and the execution time for varying TOR width T_w while fixing the number of voxels to be $75 \times 75 \times 26$ in Table V.

III.B. Image reconstruction accuracy

Transaxial slices of the hot rod phantom reconstructed using the CPU and the GPU are quantitatively identical (Fig. 7), with normalized RMS deviation between the two images being 0.05% after two iterations, which is negligible compared to the statistical variance of the voxel values in a typical PET scan (>10%, from Poisson statistics). The profile through the hot rods [Fig. 7(e)] and the contrast and noise measurements [Fig. 7(f)] are virtually the same for the two images.

A maximum intensity projection (MIP) of the mouse scanned on the GE eXplore Vista DR system[35] is shown in Fig. 8. Small features of the mouse, including the bones and the tail, are visible in both images. The normalized RMS deviation between the CPU image and the GPU image is 0.1%.

Transaxial slices of the reconstructed patient image from a Philips Gemini TF PET/CT scanner[36] using the CPU and the GPU-CUDA methods are quantitatively identical (Fig. 9). The normalized RMS deviation between slice 20 of the GPU image and the CPU image is 0.2% for non-ToF [Figs. 9(a) and 9(b)], and 0.6% for ToF [Figs. 9(c) and 9(d)], which are negligible given the statistical variance of the voxel values in a typical PET scan. The lesion contrast of the images generated using the CPU and GPU methods are 2.6 and 2.7, respectively, for non-ToF, and 3.0 and 3.1, respectively, for ToF.

TABLE III. Execution time for processing 1 million random events in an image matrix of $L \times L \times L$ with TOR width T_w increasing simultaneously with L.

L	32	48	64	128	192	256
T_w	1	2	3	6	9	12
ToF (ms)	11	17	57	509	3595	11317
Non-ToF (ms)	21	30	95	828	5962	18994

IV. DISCUSSION

The overall speed up of the GPU-CUDA method is a result of reformulating the algorithms to match both the hardware memory hierarchy and the GPU execution control flow. Among the various contributions summarized in Fig. 5, reducing global memory access through caching and improving global memory bandwidth through coalesced memory access are the most important ones. A simple GPU implementation where computation is directly mapped to GPU hardware gives only 17× speedup compared with the baseline CPU implementation, whereas a fully optimized GPU implementation using the strategies described in this paper gives more than 12× speedup on top of the simple GPU implementation.

A customized cache was used for speeding up access to the voxels. It is worth noting that the Fermi architecture has a built-in L1 cache, but since the L1 cache is a general-purpose cache optimized for a broad range of access patterns to the global memory, its performance is expected to be worse than a cache customized for a specific memory access pattern. This is verified by switching off our customized cache, which shows that the built-in L1 cache is about 5 times slower (Fig. 5) than our customized cache for our specific application.

The total throughput (measured by the number of lines processed per second) improves with increasing number of thread blocks (Fig. 6), until reaching a plateau when the number of thread blocks exceeds the number of physical streaming multiprocessors (SMs) on the GPU (i.e., 15 for

TABLE II. Effect of using fast math for one iteration of 1 million random ToF LORs in a $75 \times 75 \times 26$ image.

TOR size ($T_w \times T_w$)	Execution time saved (ms)	Percentage of execution time saved (%)	Normalized RMS deviation between two images with and without fast math
3×3	27	30.7%	1.7×10^{-6}
5×5	56	30.4%	1.3×10^{-6}
7×7	106	31.9%	0.7×10^{-6}

TABLE IV. Execution time for processing 1 million random events in an image matrix of $L \times L \times L$ with fixed TOR width 3×3.

L	32	48	64	128	256
# voxels (L^3)	3.3×10^4	1.1×10^5	2.6×10^5	2.1×10^6	1.7×10^7
ToF (ms)	29	42	57	232	1387
Non-ToF (ms)	53	73	95	367	2119

TABLE V. Execution time for processing 1 million random LORs in an image matrix of $75 \times 75 \times 26$ for different TOR width T_w. T_w^2 is the maximum number of voxels in a TOR-slice intersection.

T_w	1	3	5	7	9	11	13	15
T_w^2	1	9	25	49	81	121	169	225
ToF (ms)	24	61	128	226	360	529	731	968
Non-ToF (ms)	44	95	215	382	614	906	1256	1668

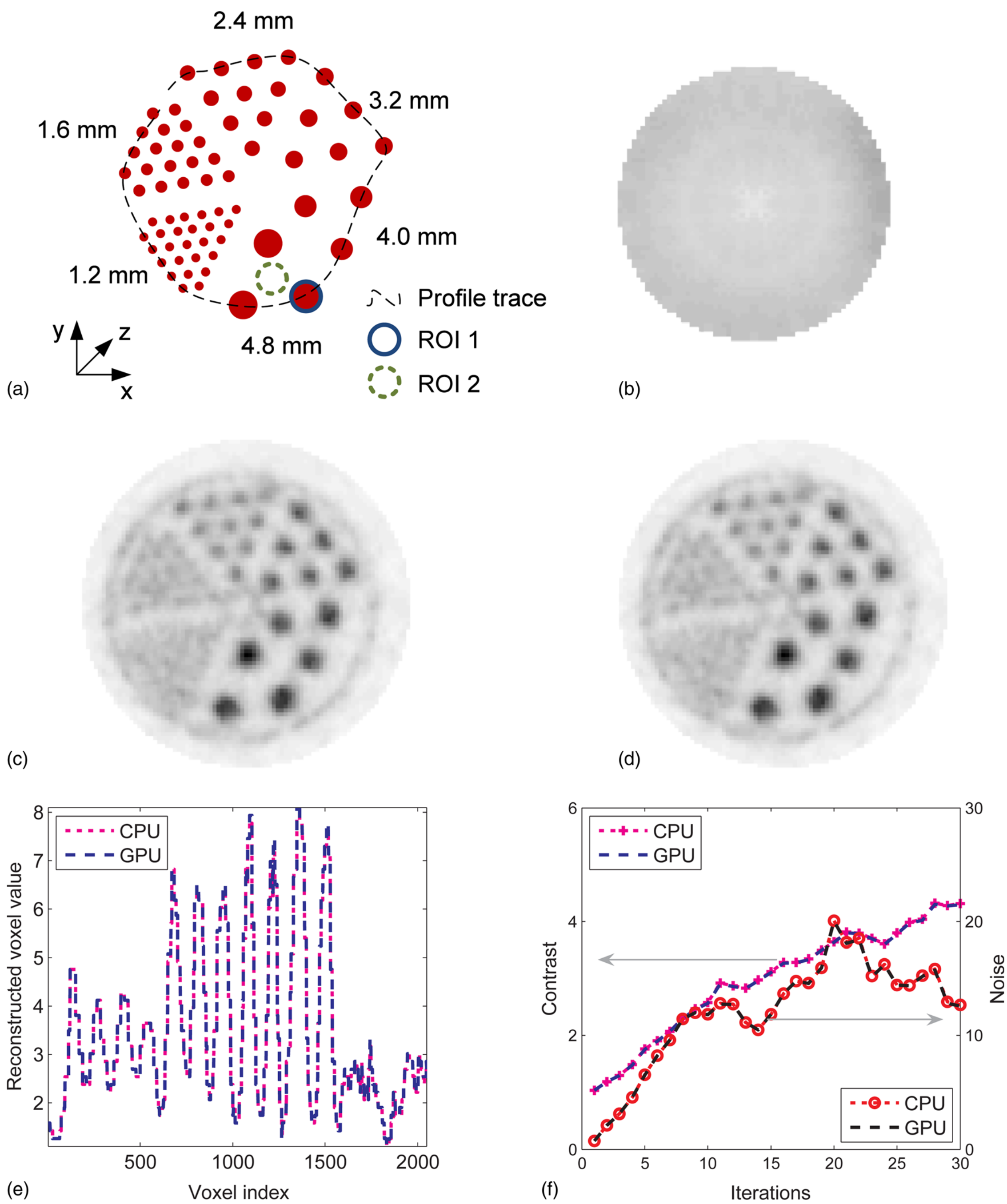

FIG. 7. Hot rod phantom (a) acquired on a preclinical PET scanner and reconstructed with 2 iterations and 40 subsets of list-mode OSEM, using (c) CPU method and (d) GPU-CUDA method. (b) The normalization map. Profiles of (c) and (d) through the centers of the hot rods, depicted in (a), are shown in (e). Contrast between the two ROIs in (a) and noise as functions of the number of iterations are shown in (f). The method for computing contrast and noise are explained in Sec. II C 3. The processing time for the GPU and the CPU is 7.0 s and 23 min, respectively.

(a) CPU image (b) GPU image

FIG. 8. Mouse PET scan (maximum intensity projection), reconstructed with three iterations and five subsets of list-mode OSEM using the CPU method (a) and the GPU-CUDA method (b). The processing time for the GPU and the CPU is 8.0 s and 28 min, respectively.

GTX 480 and 30 for GTX 285). This result is expected because when the number of thread blocks is less than the number of SMs, some of the SMs are idle, thus, the overall performance is decreased. When the number of thread blocks exceeds the number of SMs, the performance drops slightly because there is a small overhead for queuing and scheduling threads. Using the GTX 480 with 15 thread blocks each containing 1024 threads, we can achieve the peak performance of 10.5 million lines per second for non-ToF, and 16.5 million lines per second for ToF. The technological trends toward more shared memory and more processing cores, evidenced by the latest generation of GPU hardware, indicate that the GPU-CUDA method will scale well in future generations of GPUs.

Because the GPU-CUDA method has very low overhead, the performance scales linearly with the number of events (Table I). The execution time T is a linear function of the number of lines N, as described in the fitted model $T = aN + b$, where $b = 2.31$ ms gives the latency, and $a = 59.77$ ms/million gives the throughput.

Using fast math for arithmetic calculations on the GPU reduces execution time by about 17% (Fig. 5), with negligible change in image accuracy (Table II).

When the number of voxels and the width of the TOR increase proportionally, the execution time is proportional to the total number of voxels L^3 in the reconstructed image (Table III). This observed $O(L^3)$ complexity comes from two sources: the number of slices increases with L (Table IV), and the number of voxels in each slice intersected by a TOR increases with L^2 (Table V). Note that for large values of L such as 128 and 256, the size of an image slice exceeds the size of the shared memory of the GPU. The tiling mechanism we used to handle large image volumes has a small overhead, so the slow growth of the execution time is maintained (Table IV).

Note that even for large values of T_w, the execution is still quite fast (Table V, for 9×9 TOR, per-iteration execution time is 360 ms for ToF and 614 ms for non-ToF), indicating that we can incorporate broader TORs with sophisticated system modeling while still maintaining a relatively low computational cost.

The GPU-CUDA method also preserves the high accuracy of the reconstructed image data. The normalized RMS deviations between the images generated using the CPU and the GPU methods are negligible compared with the typical noise level in the PET image. We believe that the small

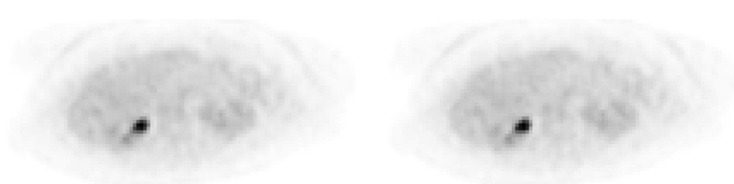

(a) CPU, non-ToF (b) GPU, non-ToF

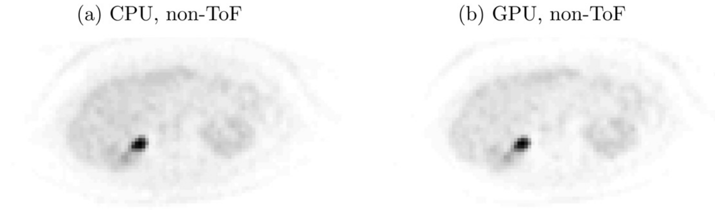

(c) CPU, ToF (d) GPU, ToF

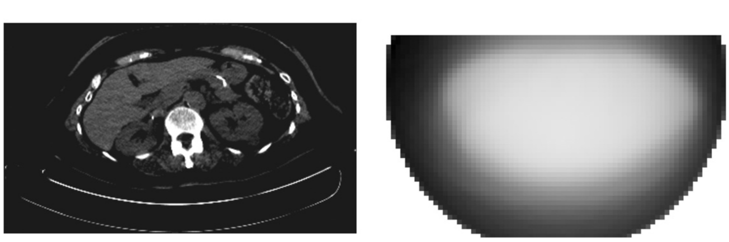

(e) Corresponding CT image (f) Normalization image

FIG. 9. Transaxial image taken through slice 30 of the liver of the reconstructed patient data from a Philips Gemini TF PET/CT scanner. A CT image at the same slice location is shown in (e) with a soft tissue window and inverse gray scale to provide an anatomical frame of reference. The (cropped) normalization image is shown in (f). The lesion is visualized with higher contrast for the ToF data. For non-ToF, the lesion contrast for the CPU and GPU methods are 2.6 and 2.7, respectively. For ToF, the values are 3.0 and 3.1, respectively. The processing time for the GPU and the CPU is 7.7 s and 42 min, respectively.

deviation we measured was caused by small variations in how the arithmetic operations are performed on the CPU and GPU. For example, we have observed that the exponential function produces slightly different results on different platforms. The fast math operations and approximate nature of the linear interpolation in texture memory in the GPU also contributes slightly to the difference. Since the image is reconstructed by solving an ill-posed inverse problem with a poorly conditioned system matrix, these small differences could be amplified.

Because the CUDA framework is design to be forward compatible with future GPUs, the proposed method can be directly applied to new generations of hardware without any modification. Of course, the performance comparison would change depending on how much faster the new GPU and CPU are compared with the ones used in the paper. However, given the speed improvement using the proposed method and the rapid development of the GPU technology, using GPU for data-intensive image reconstruction applications would still make sense, at least in the foreseeable future.

V. CONCLUSION

A list-mode time-of-flight OSEM library was developed on the GPU-CUDA platform. Our studies show that the GPU reformulation of 3D list-mode OSEM is >200 times faster than a CPU reference implementation for non-ToF reconstruction, and >300 times faster for ToF processing. This is more than 12× faster than a simple GPU implementation that does not use the optimization strategies proposed in this paper. The images produced by the GPU-CUDA method are virtually identical to those produced on the CPU.

The proposed method can be easily adapted to allow researchers to use more advanced algorithms for high resolution PET reconstruction, based on additional information such as depth of interaction (DoI) and photon energy. The GPU-CUDA method naturally supports arbitrarily broad LORs, thus can be used for more accurate reconstruction methods that incorporate shift-varying system point spread functions (PSFs).[37]

ACKNOWLEDGMENTS

The authors would like to thank Peter Olcott and Garry Chinn at Stanford University for helpful discussions and comments, and NVIDIA for providing a GTX 285 GPU. This work was sponsored by a research grant from Philips Healthcare.

[a)] Author to whom correspondence should be addressed. Electronic mail: cslevin@stanford.edu

[1] S. Surti, S. Karp, L. M. Popescu, E. Daube-Witherspoon, and M. Werner, "Investigation of time-of-flight benefit for fully 3D PET," IEEE Trans. Med. Imaging **25**, 529–538 (2006).

[2] J. S. Karp, S. Surti, Margaret E. Daube-Witherspoon, and G. Muehllehner, "Benefit of time-of-flight in PET: Experimental and clinical results," J. Nucl. Med. **49**, 462–470 (2008).

[3] S. Matej, S. Surti, S. Jayanthi, M. E. Daube-Witherspoon, R. M. Lewitt, and J. S. Karp, "Efficient 3D TOF PET reconstruction using view-grouped histo-images: DIRECT-direct image reconstruction for TOF," IEEE Trans. Med. Imaging **28**, 739–751 (2009).

[4] M. Watanabe, H. Uchida, H. Okada, K. Shimizu, N. Satoh, E. Yoshikawa, T. Ohmura, T. Yamashita, and E. Tanaka, "A high resolution PET for animal studies," IEEE Trans. Med. Imaging **11**, 577–580 (1992).

[5] S. R. Cherry, Y. Shao, R. W. Silverman, K. Meadors, S. Siegel, A. Chatziioannou, J. W. Young, W. Jones, J. C. Moyers, D. Newport, A. Boutefnouchet, T. H. Farquhar, M. Andreaco, M. J. Paulus, D. M. Binkley, R. Nutt, and M. E. Phelps, "MicroPET: A high resolution PET scanner for imaging small animals," IEEE Trans. Nucl. Sci. **44**, 1161–1166 (1997).

[6] J.-Y. Peng, J. A. D. Aston, R. N. Gunn, C.-Y. Liou, and J. Ashburner, "Dynamic positron emission tomography data-driven analysis using sparse bayesian learning," IEEE Trans. Med. Imaging **27**, 1356–1369 (2008).

[7] L. A. Shepp and Y. Vardi, "Maximum likelihood reconstruction for emission tomography," IEEE Trans. Med. Imaging **1**, 113–122 (1982).

[8] H. M. Hudson and R. S. Larkin, "Accelerated image reconstruction using ordered subsets of projection data," IEEE Trans. Med. Imaging **13**, 601–609 (1994).

[9] A. J. Reader, K. Erlandsson, M. A. Flower, and R. J. Ott, "Fast accurate iterative reconstruction for low-statistics positron volume imaging," Phys. Med. Biol. **43**, 835–846 (1998).

[10] L. Parra and H. H. Barrett, "List-mode likelihood: EM algorithm and image quality estimation demonstrated on 2-D PET," IEEE Trans. Med. Imaging **17**, 228–235 (1998).

[11] L. M. Popescu, S. Matej, and R. M. Lewitt, "Iterative image reconstruction using geometrically ordered subsets with list-mode data," *Nuclear Science Symposium Conference Record*, Vol. 6 (IEEE, Rome, Italy, 2004), pp. 3536–3540.

[12] A. Rahmim, M. Lenox, A. J. Reader, C. Michel, Z. Burbar, T. J. Ruth, and V. Sossi, "Statistical list-mode image reconstruction for the high resolution research tomograph," Phys. Med. Biol. **49**, 4239 (2004).

[13] G. Pratx, P. D. Olcott, G. Chinn, and C. S. Levin, "Fast, accurate and shift-varying line projections for iterative reconstruction using the GPU," IEEE Trans. Med. Imaging **28**, 435–445 (2009).

[14] I. K. Hong, S. T. Chung, H. K. Kim, Y. B. Kim, Y. D. Son, and Z. H. Cho, "Ultra fast symmetry and SIMD-based projection-backprojection (SSP) algorithm for 3D PET image reconstruction," IEEE Trans. Med. Imaging **26**, 789–803 (2007).

[15] F. Xu and K. Mueller, "Accelerating popular tomographic reconstruction algorithms on commodity PC graphics hardware," IEEE Trans. Nucl. Sci. **52**, 654–663 (2005).

[16] F. Xu and K. Mueller, "Real-time 3D computed tomographic reconstruction using commodity graphics hardware," Phys. Med. Biol. **52**, 3405 (2007).

[17] H. G. Hofmann, B. Keck, C. Rohkohl, and J. Hornegger, "Comparing performance of many-core CPUs and GPUs for static and motion compensated reconstruction of C-arm CT data," Med. Phys. **38**, 468–473 (2011).

[18] F. Xu, A. Khamene, and O. Fluck, "High performance tomosynthesis enabled via a GPU-based iterative reconstruction framework," Proc. SPIE **7258**, pp. 72585A (2009).

[19] R. Jacques, J. Wong, R. Taylor, and T. McNutt, "Real-time dose computation: GPU-accelerated source modeling and superposition/convolution," Med. Phys. **38**, 294–305 (2011).

[20] S. Hissoiny, B. Ozell, H. Bouchard, and P. Despres, "GPUMCD: A new GPU-oriented Monte Carlo dose calculation platform," Med. Phys. **38**, 754–764 (2011).

[21] G. Pratx and L. Xing, "GPU computing in medical physics: A review," Med. Phys. **38**, 2685–2697 (2011).

[22] Z. Hu, W. Wang, E. E. Gualtieri, M. J. Parma, E. S. Walsh, D. Sebok, Y. L. Hsieh, C. H. Tung, J. J. Griesmer, J. A. Kolthammer, L. M. Popescu, M. Werner, J. S. Karp, A. Bucur, J. van Leeuwen, and D. Gagnon, "Dynamic load balancing on distributed listmode time-of-flight image reconstruction," *IEEE Nuclear Science Symposium Conference Record* (IEEE, San Diego, California, 2006), pp. 3392–3396.

[23] NVIDIA, NVIDIA CUDA Programming Guide 3.0 (2010).

[24] E. Veklerov, J. Llacer, and E. J. Hoffman, "MLE reconstruction of a brain phantom using a Monte Carlo transition matrix and a statistical stopping rule," IEEE Trans. Nucl. Sci. **35**, 603–607 (1988).

[25] R. H. Huesman, G. J. Klein, W. W. Moses, J. Qi, B. W. Reutter, and P. R. G. Virador, "List-mode maximum-likelihood reconstruction applied to positron emission mammography (PEM) with irregular sampling," IEEE Trans. Med. Imaging **19**, 532–537 (2000).

[26]C. A. Johnson, Y. Yan, R. E. Carson, R. L. Martino, and M. E. Daube-Witherspoon, "A system for the 3D reconstruction of retracted-septa PET data using the EM algorithm," *Nuclear Science Symposium and Medical Imaging Conference Record*, Vol. 3 (IEEE, Norfolk, Virginia, 1994), pp. 1325–1329.
[27]J. Qi, R. M. Leahy, S. R Cherry, A. Chatziioannou, and T. H. Farquhar, "High-resolution 3D bayesian image reconstruction using the microPET small-animal scanner," Phys. Med. Biol. **43**, 1001 (1998).
[28]L. Zhang, S. Staelens, R. V. Holen, J. D. Beenhouwer, J. Verhaeghe, I. Kawrakow, and S. Vandenberghe, "Fast and memory-efficient Monte Carlo-based image reconstruction for whole-body PET," Med. Phys. **37**, 3667–3676 (2010).
[29]R. L. Siddon, "Fast calculation of the exact radiological path for a three-dimensional CT array," Med. Phys. **12**, 252–255 (1985).
[30]P. M. Joseph, "An improved algorithm for reprojecting rays through pixel images," IEEE Trans. Med. Imaging **1**, 192–196 (1982).
[31]G. Pratx and C. Levin, "Online detector response calculations for high-resolution PET image reconstruction," Phys. Med. Biol. **56**, 4023 (2011).
[32]S. Matej and R. M. Lewitt, "Practical considerations for 3D image reconstruction using spherically symmetric volume elements," IEEE Trans. Med. Imaging **15**, 68–78 (1996).
[33]P. Aguiar, M. Rafecas, J. E. Ortuño, G. Kontaxakis, A. Santos, J. Pavía, and D. Ros, "Geometrical and Monte Carlo projectors in 3D PET reconstruction," Med. Phys. **37**, 5691–5702 (2010).
[34]M. Herlihy and N. Shavit, *The Art of Multiprocessor Programming* (Morgan Kaufmann, Waltham, Massachusetts, 2008).
[35]Y. Wang, J. Seidel, B. M. W. Tsui, J. J. Vaquero, and M. G. Pomper, "Performance evaluation of the GE Healthcare eXplore VISTA dual-ring small-animal PET scanner," J. Nucl. Med. **47**, 1891–1900 (2006).
[36]S. Surti, A. Kuhn, M. E. Werner, A. E. Perkins, J. Kolthammer, and J. S. Karp, "Performance of Philips Gemini TF PET/CT scanner with special consideration for its time-of-flight imaging capabilities," J. Nucl. Med. **48**, 471–480 (2007).
[37]A. M. Alessio, C. W. Stearns, S. Tong, S. G. Ross, S. Kohlmyer, A. Ganin, and P. E. Kinahan, "Application and evaluation of a measured spatially variant system model for PET image reconstruction," IEEE Trans. Med. Imaging **29**, 938–949 (2010).